symmetry

IMPACT FACTOR 2.2

CITESCORE 5.4

Article

Towards a Warm Holographic Equation of State by an Einstein–Maxwell-Dilaton Model

Rico Zöllner and Burkhard Kämpfer

MDPI

https://doi.org/10.3390/sym16080999

symmetry

MDPI

Article

Towards a Warm Holographic Equation of State by an Einstein–Maxwell-Dilaton Model

Rico Zöllner [1,*,†] and Burkhard Kämpfer [2,3,†]

[1] Institut für Technische Logistik und Arbeitssysteme, TU Dresden, 01062 Dresden, Germany
[2] Helmholtz-Zentrum Dresden-Rossendorf, 01314 Dresden, Germany; kaempfer@hzdr.de
[3] Institut für Theoretische Physik, TU Dresden, 01062 Dresden, Germany
* Correspondence: rico.zoellner@tu-dresden.de
† These authors contributed equally to this work.

Abstract: The holographic Einstein–Maxwell-dilaton model is employed to map state-of-the-art lattice QCD thermodynamics data from the temperature (T) axis towards the baryon–chemical potential (μ_B) axis and aims to gain a warm equation of state (EoS) of deconfined QCD matter which can be supplemented with a cool and confined part suitable for subsequent compact (neutron) star (merger) investigations. The model exhibits a critical end point (CEP) at $T_{\mathrm{CEP}} = \mathcal{O}(100)$ MeV and $\mu_{B\,\mathrm{CEP}} = 500 \ldots 700$ MeV with an emerging first-order phase transition (FOPT) curve which extends to large values of μ_B without approaching the μ_B axis. We consider the impact and peculiarities of the related phase structure on the EoS for the employed dilaton potential and dynamical coupling parameterizations. These seem to prevent the design of an overall trustable EoS without recourse to hybrid constructions.

Keywords: holographic Einstein–Maxwell-dilaton model; critical end point; equation of state

check for updates

Citation: Zöllner, R.; Kämpfer, B. Towards a Warm Holographic Equation of State by an Einstein–Maxwell-Dilaton Model. *Symmetry* **2024**, *16*, 999. https://doi.org/10.3390/sym16080999

Academic Editor: Dubravko Klabučar

Received: 18 June 2024
Revised: 10 July 2024
Accepted: 12 July 2024
Published: 6 August 2024

1. Introduction

The advent of detecting gravitational waves of merging neutron stars [1] and improved determinations of mass–radius relations of neutron stars, e.g., by NICER [2–4], has triggered a cascade of related investigations, most notably focused on accessing the cool equation of state (EoS) of dense strong-interaction matter. Among the various approaches to compact (neutron) star EoS is the application of the famous AdS/CFT correspondence, which mimics dense matter by a suitable gravity dual of QCD [5–7]. Here, we employ such a holographic approach based on the Einstein–Maxwell-dilaton (EMd) model pioneered in [8,9] and used further in [10–21]. References [22,23] provide a survey of and a valuable comparison between of Dirac–Born–Infeld AdS/CFT models.

Our motivation is as follows: Given lattice QCD thermodynamics results, e.g., the scaled pressure, p/T^4, on the temperature (T) axis [24,25] supplemented with the susceptibility $\chi_2 = \partial^2 p / \partial \mu_B^2 |_{\mu_B = 0}$ [26], the EMd model primarily delivers the entropy density $s(T, \mu_B)$ and the baryon density $n_B(T, \mu_B)$, which can be integrated to arrive at the potential $p(T, \mu_B)$ (even at $\mu_B = 0$, $p(T, \mu_B = 0) = p(T_{min}) + \int_{T_{min}}^{T} \mathrm{d}\bar{T} s(\bar{T})$ is a nonlocal quantity which needs $p(T_{min})$ as input parameter, supposing that $s(T \geq T_{min}, \mu_B = 0)$ is accurately given. More favorable is to directly use $p(T, \mu_B = 0)$ from lattice QCD results and map it without further assumptions into the T-μ_B plane, as advocated below). These quantities additionally depend on the baryon–chemical potential μ_B. The lattice input [24] is provided, at $\mu_B = 0$, for $T \in [T_1, T_2] = [125, 240]$ MeV and allows the adjustment of the dilaton potential and the dynamical coupling of the EMd model. The lattice data [24] for $\mu_B / T = 0.5, 1, \ldots, 3.5$ serve as a control, again with $T \in [125, 240]$ MeV for 2+1 flavors (for other relevant lattice datasets, cf. [27–29]). Curves of $p(T, \mu_B) = const$, i.e., isobars, can then be utilized to continue the lattice-given EoS $p(T, \mu_B = 0)$ into the T-μ_B plane, and finally—if no obstacle is met—to $p(T = 0, \mu_B)$. That is, the EoS—here, the pressure—is directly mapped from the T axis on the μ_B axis. Curves of $p(T,\mu_B) = const$ are determined by solving

$$\left.\frac{\mathrm{d}T(\mu_B)}{\mathrm{d}\mu_B}\right|_{p=const} = -\frac{n_B(T,\mu_B)}{s(T,\mu_B)}, \tag{1}$$

where the inverse entropy-per-baryon determines the slope field. Solutions are $T(\mu_B)|_{p=p_0}$ with $T(\mu_B=0)|_{p=p_0} = T_0$ and $p(T_0,\mu_B=0) = p_0$. Via Gibbs–Duhem equation, the energy density (e) follows from $e = -p + sT + n_B\mu_B$.

The gained cool EoS $p(e)$ can be then used as input for compact (neutron) star calculations. This vision is illustrated in Figure A1 in Appendix A with a toy model. The abovementioned state-of-the-art lattice data uncovers, in fact, a relevant pressure interval: $p(T_1,\mu_B = 0) = \mathcal{O}(10^1)$ MeV/fm^3 and $p(T_2,\mu_B = 0) = \mathcal{O}(10^3)$ MeV/fm^3. For the toy model, these values translate into $p(T = 0,\mu_{B1}) = \mathcal{O}(10^1)$ MeV/fm^3 and $p(T = 0,\mu_{B2}) = \mathcal{O}(10^3)$ MeV/fm^3 localized just above the reliable pressure interval accessible by nuclear-physics many-body methods (cf. Figure 1 in [30,31] and Figure 12 in [32] which suggest the matching point to be at about 3 MeV/fm^3 (pressure) and 200 MeV/fm^3 (energy density)). The corresponding energy densities $e(T = 0,\mu_{B1})$ and $e(T = 0,\mu_{B2})$ depend, of course, on the details of the mapping along $p = const$ curves from the T axis to the μ_B axis, as do the actual values of $\mu_{B1,2}$.

However, such a vision meets potential obstacles. These are (i) already for $\mu_B = 0$, an unwanted first-order or Hawking–Page phase transition may occur outside the controlled region $T \in [T_1, T_2]$, where $T_{1,2}$ are again the lower and upper limits of the safe EoS, which are used to adjust dilaton potential and dynamical coupling of the EMd model; (ii) a critical end point (CEP) and related first-order phase transition (FOPT) curve may disturb the expected pattern of curves $T(\mu_B)|_{p=const}$, displayed in Appendix A for the toy model; and (iii) the expected pattern of curves $T(\mu_B)|_{p=const}$ does not continue smoothly to the μ_B axis. In fact, item (i) is met in [13] ($T_{\mathrm{FOPT}}(\mu_B = 0) \approx 45$ MeV), which focuses on the neighborhood of a CEP at $\mu_B > 0$, and in [11] ($T_{\mathrm{FOPT}}(\mu_B = 0) \approx 1$ MeV). The occurrence of a CEP at $\mu_B > 0$ is known [8,9] and a welcome effect to study. Within such a model class is its impact on the EoS and related dynamics, thus explicating the conjecture posed in [33–36] and motivating a continuation of the ongoing energy scan at RHIC [37,38]. (For the tight connection of heavy ion–neutron star physics, cf. [39,40].)

To avoid irritations by item (i), we optionally impose here novel side conditions for the dilaton potential. It happens that this enforces parameterizations which facilitate a change of the FOPT curve below the CEP from convex to concave, i.e., the FOPT curve levels off and seems to asymptotically approach to the μ_B axis, thus hindering a concise cool EoS prediction. Nevertheless, the warm EoS, characterized by $p(e)|_T$ or the scaled trace anomaly/conformality measure $\Delta(e)|_T := (e - 3p)/(3e)|_T$ [41,42], is accessible and may be useful for numerical studies.

While many preceding EMD studies focus on the CEP localization and/or transport coefficients near the CEP and across the FOPT curve, here, we place emphasis on the EoS. Among the hitherto less discussed issues is the pattern of isentropes near the CEP and FOPT. In [13], it has been pointed out that the isentropes, with respect to "incoming" and "outgoing" under adiabatic expansion, in various EMd models can be fairly different. A general classification of such isentropic patterns was proposed recently in [43]. Such a study and holographic perspective is of relevance for heavy-ion collisions experiments and speculations on sourcing stochastic gravitation waves in the cosmic confinement transition [44,45].

Our paper is organized as follows. We recap the EMd model and its data adjustment in Section 2. Numerical results are presented in Section 3, where we discuss the CEP position, the shape of the FOPT curve up to fairly large values of μ_B, the shape of the $p = const$ curves, and a closer inspection of the resulting EoS by means of various contour plots and related cross-sections of thermodynamic quantities. We conclude and summarize in Section 4. A brief series of appendices complements our analysis. Appendix A sketches our vision of mapping QCD data from the T axis into the T-μ_B plane, and Appendix B supplements details of the EMd model used. Appendix C considers the density and pressure near and across the FOPT curve. Appendix D presents a numerical study of a new dilaton potential parameterization adjusted to data, which allows for the construction of a χ^2 landscape.

2. Holographic Einstein–Maxwell-Dilaton Model

In line with [8,11,12] we employ the EMd action (reference [6] relates the EMd model (2) to a D3-D7 action and Taylor-expanded versions of string theory-anchored approaches. Hadron, nucleon, and quark degrees of freedom are added separately in [21]) in a fiducial five-dimensional pseudo-Riemann spacetime with asymptotic AdS symmetry:

$$S_{\mathrm{EMd}} = \frac{1}{2\kappa_5^2} \int \mathrm{d}^4x\, \mathrm{d}r\, \sqrt{-g_5} \left(R - \frac{1}{2} \partial^M \phi\, \partial_M \phi - V(\phi) - \frac{1}{4} \mathcal{G}(\phi) F_{\mathcal{B}}^2 \right), \tag{2}$$

where R denotes the Einstein–Hilbert gravity part, and $F_{\mathcal{B}}^{MN} = \partial^M \mathcal{B}^N - \partial^N \mathcal{B}^M$ stands for the field strength tensor of an Abelian gauge field $\mathcal{B}$ à la Maxwell with $\mathcal{B}_M \mathrm{d}x^M = \Phi(r)\,\mathrm{d}t$ defining the electrostatic potential. An embedded black hole facilitates the description of a hot and dense medium (due to its Hawking surface temperature) and sources an electric field, thus holographically encoding a temperature and an entropy density of the system. Dynamical objects are the scalar dilaton field ϕ and a Maxwell-type field Φ which are governed by a dilaton potential $V(\phi)$, a dynamical coupling $\mathcal{G}(\phi)$, and the spacetime which is described by the line element squared

$$\mathrm{d}s^2 = g_{MN} \mathrm{d}x^M \mathrm{d}x^N = e^{2A(r)} \left(-f(r) \mathrm{d}t^2 + \mathrm{d}\vec{x}^{\,2} \right) + \frac{\mathrm{d}r^2}{f(r)}, \tag{3}$$

where $r = 0$ is the horizon position, $r \in [0, \infty]$ the radial coordinate, A the warp factor, and f the blackness function. The resulting Einstein equations are a set of coupled second-order ODEs to be solved with appropriate boundary conditions; see Appendix B. Within the present bottom-up approach, the quantities V and $\mathcal{G}$ are tuned ("tuning" within the bottom-up approach faces three issues: choices of the functional forms of V and $\mathcal{G}$ and parameter adjustments at data. For Bayesian analyses cf. [46]) to reproduce the lattice QCD data [24,47] for 2+1 flavor strong-interaction matter (quark–gluon plasma).

Our ansätze for the dilaton potential V and dynamical coupling $\mathcal{G}$ are

$$\mathcal{W} \equiv \partial_\phi \ln V(\phi) = (p_1 \phi + p_2 \phi^2 + p_3 \phi^3) \exp\{-\gamma \phi\}, \tag{4}$$

$$\mathcal{G}(\phi) = \frac{1}{1 + c_3} \left(\frac{1}{\cosh(c_1 \phi + c_2 \phi^2)} + \frac{c_3}{\cosh c_4 \phi} \right) \tag{5}$$

with parameters $\{p_{1,2,3}\} = \{0.165919, 0.269459, -0.017133\}$, $\gamma = 0.471384$, and $\{c_{1,2,3,4}\} = \{-0.276851, 0.394100, 0.651725, 101.6378\}$; the prefactor $1/(1 + c_3)$ ensures $\mathcal{G}(\phi = 0) = 1$. The scale is set by $L^{-1} = 216$ MeV, in $L^2 V(\phi) = -12 \exp\{\int_0^\phi \mathrm{d}\tilde{\varphi} \mathcal{W}(\tilde{\varphi})\}$ and $\kappa_5 = 1.87 L^{3/2}$ is used. The conditions (i) $\lim_{\phi \to \infty} \mathcal{W}(p_3 > 0) = 0$ and (ii) monotony of V towards the boundary exclude a purely thermal phase transition at $\mu_B = 0$, cf. [48,49]. The parameters chosen here facilitate a smooth shape of $\mathcal{W}$ with maximum of 0.605 at $\phi = 3.373$ and a zero at $\phi = 16.321$, which corresponds to an exceedingly small temperature far below 1 MeV. Appendix D presents more details on the impact of the dilaton potential.

In contrast to former work, here, we place emphasis on the optional side condition $p_3 > 0$ which ensures that, at $\mu_B = 0$, no phase transition is facilitated outside the temperature range uncovered by the lattice data. Details of our handling of the EMd model are relegated to the Appendix B.

Despite the richness of the dataset [24], only in scarce cases is a direct comparison with our EoS results exhibited in various figures below possible. We therefore present in Figure 1 a more detailed comparison focused on $T \in [100, 250]$ MeV and for $\mu_B/T = 0.5, \ldots, 3.0$.

While the scaled pressure (left column) seems to perfectly agree, the scaled baryon density (middle column) points to some tension, in particular for larger values of μ_B/T, as already noticed in [11] and stressed in [10]. This calls for an improved dynamical coupling ansätze.

However, we could also argue for the failure of the model when extending it into the confinement region, in particular towards lower temperatures being of relevance for compact star physics. This is in line with statements in [11]. Thus, one could scrutinize the implications of the critical end point and related first-order phase transition which emerge in the EMd model for parameterizations employed hitherto in the literature. Reference [19] sharpens the above warning, further enhanced by statements in [23] ("…, the fact that the present EMD model is in good quantitative agreement with the latest lattice QCD data at finite baryon density does not automatically guarantee that the predictions made for regions of the QCD phase diagram well beyond the reach of current lattice simulations are phenomenologically reliable. Indeed, the fact that the EMD model of Ref. [10] is also able to obtain a good quantitative agreement with lattice QCD thermodynamics at zero and finite baryon density, while still predicting the QCD CEP at a significantly different location than in our model, shows that the available lattice data is not enough to strongly constraint such a prediction in the EMD class of holographic models." Further critical remarks on specific limitations and drawbacks of the holographic EMd model, see [22]).

Completing the discussion of Figure 1, we mention that s/T^3 (not displayed) is in similarly good agreement with data to p/T^4. The resulting energy density, in particular, when displayed as the ratio e/p (right column), again displays some deviations: the EMd model does not reproduce the apparent structures of the data when ignoring the error bars; including them (not displayed) makes such structures much less pronounced. Note the slight increase of the peak of e/p and its left-shift with increasing values of μ_B/T. Recap also the relations of e/p to the conformality measure $e/p = (\frac{1}{3} - \Delta)^{-1}$ and the scaled trace anomaly $(e - 3p)/T^4 = (p/T^4)(e/p - 3)$.

The dimensionless susceptibility $\chi_2(T)$ is compared successfully to precision lattice data in Figure 7 (right) in [50].

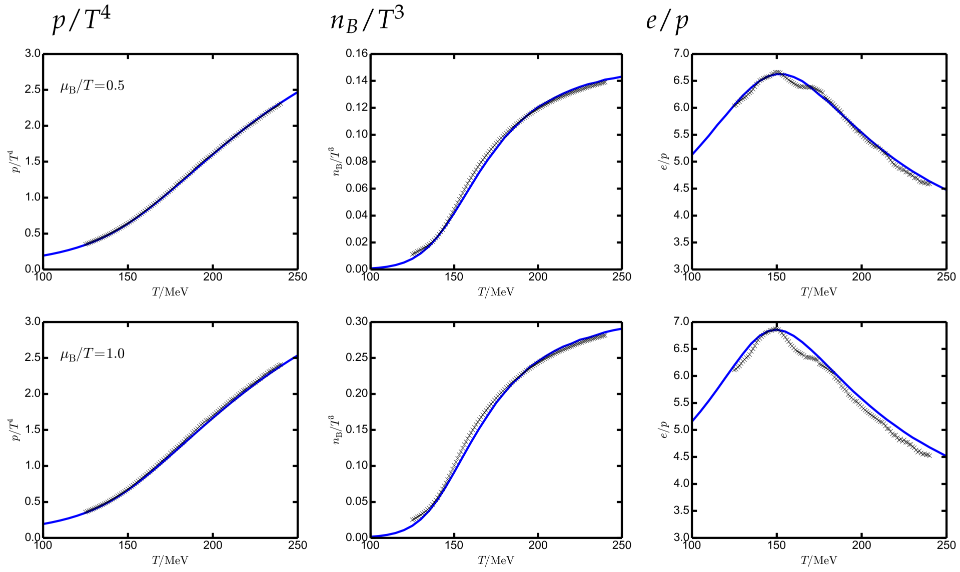

Figure 1. *Cont.*

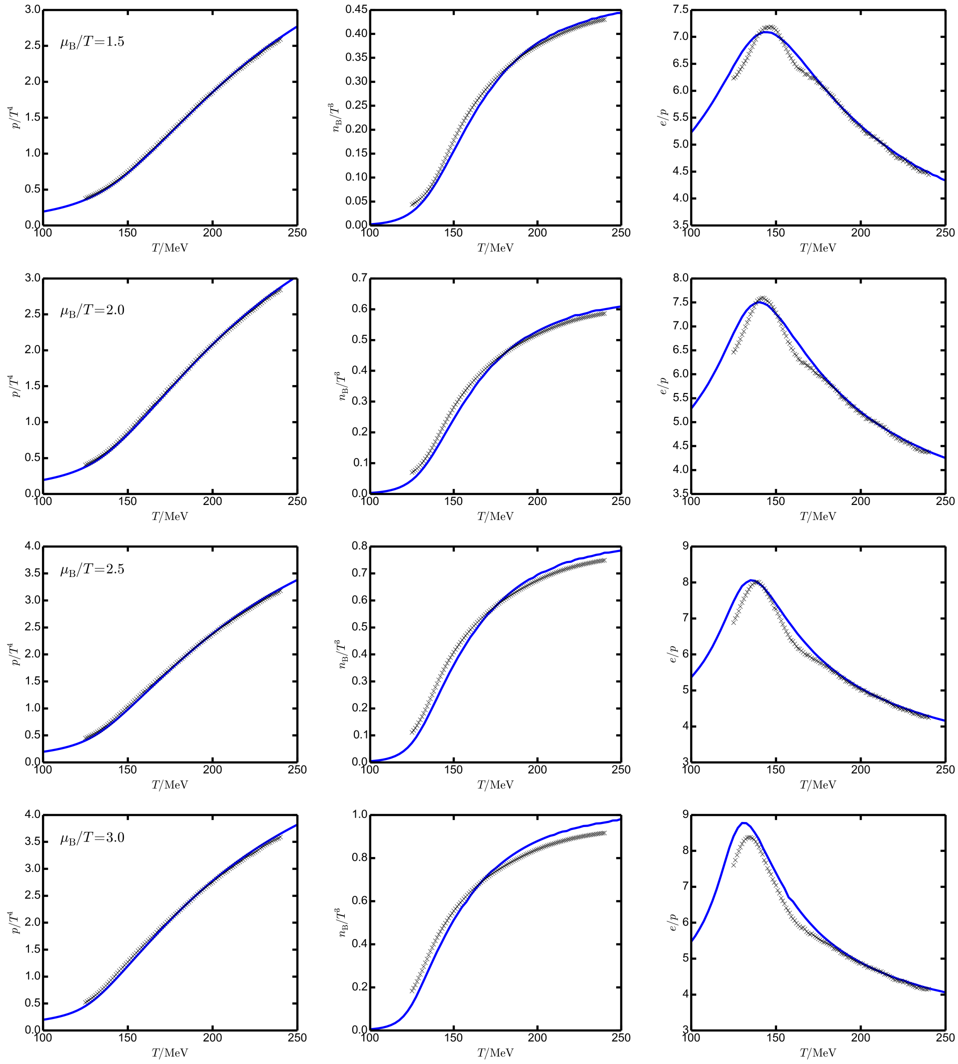

Figure 1. Comparison of the EMd model results with lattice data [24] (crosses) for $\mu_B/T = n/2$, $n = 1$ (top), ..., 6 (bottom): p/T^4 (left column), n_B/T^3 (middle column), and e/p (right column) as a function of T. Note the different scales for n_B/T^3 and e/p.

3. Numerical Results: EoS

3.1. CEP Location and FOPT

The employed parameterizations of V and $\mathcal{G}$ facilitate a CEP with coordinates $T_{\text{CEP}} = 97.2$ MeV and $\mu_{B\,\text{CEP}} = 694.7$ MeV (fat bullet) (similar CEP locations are obtained in [8,11–13]. Interestingly, QCD-functional methods deliver fairly consistent values, cf. [51], and for finite-volume effects [52]. CEP and FOPT loci are inherent in the present model, steered by the parameterizations of V and $\mathcal{G}$, in contrast, e.g., to the approach in [53,54] which allows for a free choice) and an FOPT curve $T_{\text{FOPT}}(\mu_B)$ as exhibited in Figures 2 and 3. Remarkably, the FOPT curve displays a concave shape near the CEP (as in [8,11–13]; note the agreement of $T_{\text{FOPT}}(\mu_B = 1000 \text{ MeV}) \approx 55$ MeV with Figure 11 in [11]) which, however, turns, for larger values of μ_B, into a convex shape, obviously asymptotic to the μ_B axis with dramatic consequences for the cool EoS. Our numerically accessible domain is by far larger than that of [11].

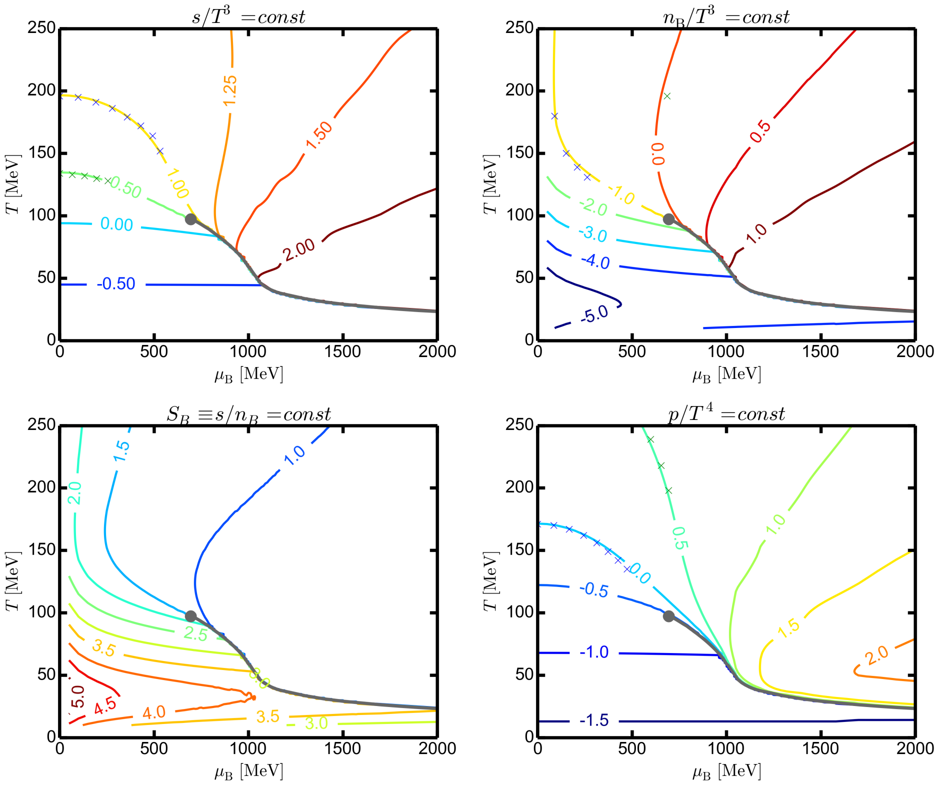

Figure 2. Contour plots of scaled entropy density s/T^3 (**left top panel**), baryon density n_B/T^3 (**right top panel**), entropy per baryon s/n_B (**left bottom panel**, relevant for adiabatic expansion), and pressure p/T^4 (**right bottom panel**) over the T-μ_B plane. The CEP is depicted as a bullet and the solid black curve is the emerging FOPT. The labeling numbers "N" mean 10^N of the respective quantity. Note the weak dependence of s/T^3 and p/T^4 on μ_B to the left of the FOPT at $T < 100$ MeV. The crosses depict results of the lattice QCD calculations [24]. The scaled energy density, $e/T^4 = -p/T^4 + s/T^3 + (\mu_B/T) n_B/T^3$, can be inferred from the displayed information.

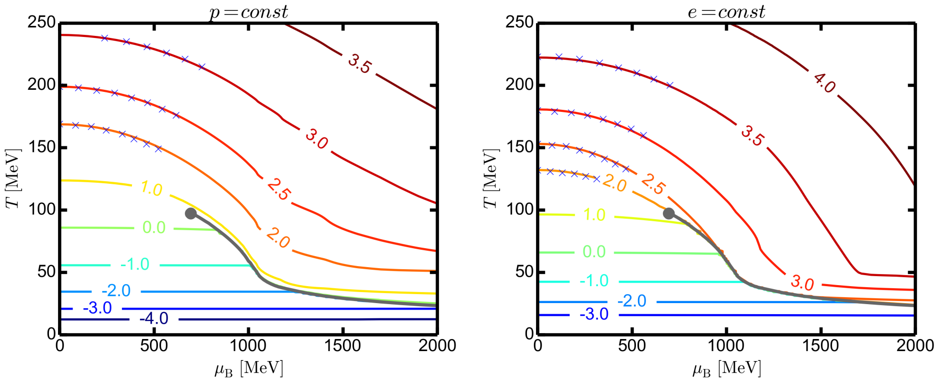

Figure 3. Contour plot of the EoS as isobars $p(T, \mu_B) = const$ (**left panel**) and iso-energy density curves $e(T, \mu_B) = const$ (**right panel**) over the T-μ_B plane. The CEP, FOPT, line style, and meaning of labeling (here in units of MeV/fm^3) are as in Figure 2. Note again the weak dependence on μ_B to the left of the FOPT at $T < 100$ MeV. The crosses depict results of the lattice QCD calculations [24].

3.2. Scaled Entropy, Density, Pressure, and Specific Entropy

The contour plots of s/T^3, n_B/T^3, s/n_B and p/T^4 exhibited in Figure 2 point to a mysteriously weak dependence of s/T^3 and p/T^4 on μ_B to the left and below the FOPT (the contour plot of n_B/T^3 (right top panel) can be used to construct the unstable region in a T vs. n_B diagram: A given point (T, μ_B) on the FOPT curve $T_{\rm FOPT}(\mu_B)$ leads to two values of the density, $n_B^{\pm}(T) := n_B(T, \mu_B)|_{T = T_{\rm FOPT}(\mu_B) \pm \epsilon}$. The unstable region has a maximum at

T_{CEP}, where $n_B^{\pm}(T_{\mathrm{CEP}})$ merge. The left-hand side flank, i.e., for the smaller values of $n_B(T)$, may be more or less steep, depending on details of the underlying model setup. Figure 4 in [13] exhibits that the slopes of isentropes are either to bypass the unstable region or enter and exit it for not too small values of s/n_B. As noted in [13], the examples in [8,9] are such to enter also the unstable region on the left-hand side without graceful exit. Subtle deformations of the isentropic trajectories and/or the left-hand side of the unstable region (e.g., by a bumpy structure) may cause a more involved picture with bypassing and entering-only and entering-and-exiting trajectories). Additionally, the quantities s/T^3, n_B/T^3, and s/n_B jump across the FOPT, while p/T^4 is continuous. The right-hand side continuations of the left-hand side iso-lines, e.g., $p/T^4 = 10^{-0.5}$ and 10^{-1}, are not visible on the displayed scale; they are squeezed into a narrow corridor between the FOPT curve and the hardly visible curve $p/T^4 = 10$ (see Appendix C for some details). The agreement of the EMd model results and lattice data [24] (crosses, error bars are ignored here and below), whenever possible, looks near-perfect (see also Figure 8 in [50]).

We emphasize the pattern of isentropic trajectories, $s/n_B = const$ (left bottom panel), which points to a nonmonotonic specific entropy at the low-temperature side in the proposed classification of [43]. The pattern is qualitatively analogous to the one of [8,9] but different to that found in [13], where “outgoing” isentropic trajectories are attributed to “incoming” trajectories across the FOPT upon adiabatic expansion. It seems that various “good fits” of the same lattice data can deliver quite different contours of $s/n_B = const$, even though we did not attempt here a dedicated χ^2 optimization with our dilaton potential and dynamical coupling parameterizations. Curves $e(T, \mu_B) = const$ are determined by $\frac{\mathrm{d}T(\mu_B)}{\mathrm{d}\mu_B}|_{e=const} = -(T\partial s/\partial\mu_B + \mu_B\partial n_B/\partial\mu_B)/(T\partial s/\partial T + \mu_B\partial n_B/\partial T)$.

3.3. Isobars and Iso-Energy Lines

The pattern of the isobars, see left panel in Figure 3, strongly deviates from the naive expectations shown in Figure A1 for the toy model. Neither left nor right of the FOPT, does one recognize a near-vertical dropping of the curves $p = const$. Instead, the mysterious low-temperature–low-μ_B behavior of the scaled pressure exhibited in the right panel of Figure 2 is retained, and, most importantly for our goals, the FOPT curves seem to repel the isobars. Thus, a smooth continuation of curves $p = const$ to the μ_B axis is hindered in the explored range. A warm EoS at $T > 50$ MeV is conceivable by our approach, but the envisaged cool EoS at small or zero temperature remains elusive. Also in the current case, the agreement with lattice data [24] (crosses) looks fine.

3.4. Warm EoS

To illustrate further features of the obtained EoS, we exhibit in Figure 4 (left panel) energy density e and pressure p_0 as functions of temperature T along the isobars $T(\mu_B)|_{p=p_0}$ (or $\mu_B(T)|_{p=p_0}$ by inversion) for various values of T_0, which generate $p_0 = p(T_0, \mu_B = 0)$. That is, the EoS in parametric form, $e(T, \mu_B(T)|_{p=p_0})$ and $p(T, \mu_B(T)|_{p=p_0})$, can be inferred from this information on e/p due to the log scale. Note the relation to the trace anomaly measure [41] via $e/p = 1/(\frac{1}{3} - \Delta)$) or $p(e)$ (see right panel). As mentioned above, the envisaged access to the small-T region is hampered by the failed approach of isobars down to the baryon–chemical potential axis, even for the “safer” isobars emerging from or running through the T-μ_B region uncovered by the lattice QCD results [24]. We stress the enormous stiffness of the EOS on the right-hand side of the FOPT. In line with the peculiar features of the EoS at $T < T_{\mathrm{CEP}}$ and matter properties for the left-hand side of the FOPT is the huge energy density jump.

The connection of the holographic EoS with the nuclear-physics-based EoS at a certain matching point requires a special treatment, beyond the goal of the present paper. Analogously, the transit to the perturbative QCD regime above about 4×10^3 MeV/fm^3 (pressure) and 1.3×10^4 MeV/fm^3 (energy density) also requires separate work. As a guideline, one could follow the construction of a hybrid EoS in the spirit of Figure 15 in [5] and plug in the present holographic EoS as one building block among others. However, we find that, at a given energy density, e.g., 10^3 MeV/fm^3, our pressure seems too low for $T < 100$ MeV in comparison with currently advocated credible EoSs, cf. Figure 1 in [30,31].

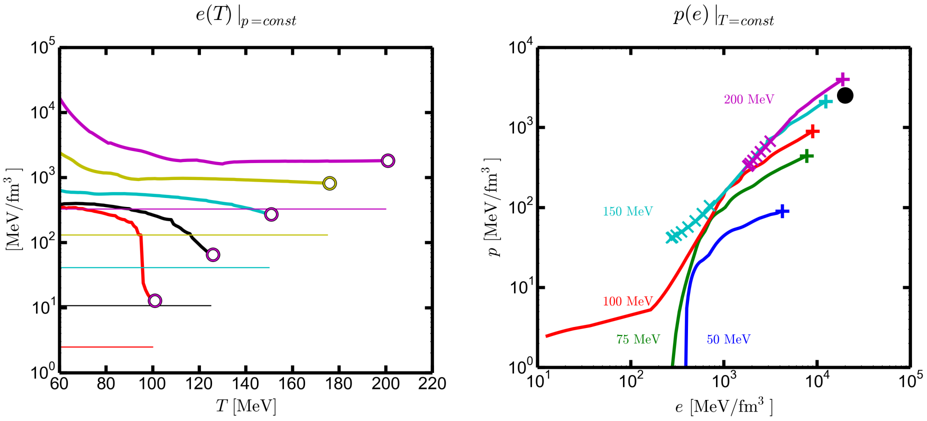

Figure 4. (**Left panel**): Energy density e (solid curves) as a function of temperature T along the "safe" isobars $T(\mu_B)|_{p=p_0}$ (see Figure 3—left) for various values of $T_0 = 125$ (black), 150 (cyan), 175 (yellow), and 200 MeV (magenta), and, thus, $p_0 = p(T_0, \mu_B = 0)$. In addition, the case of a "less reliable" isobar with $T_0 = 100$ MeV is also displayed (red). The right-hand side endpoints ("o") are for $\mu_B = 0$, both for e and pressure $p = p_0$ (horizontal thin lines with the same color code as the corresponding energy density). The difference of e and p (both in units of MeV/fm^3) in the employed log scale delivers directly e/p as a function of T along the respective isobar. Equally well, e and p for a selected constant value of T can be read off, thus providing the iso-thermal EoS $p(e)|_{T=const}$, exhibited in the (**right panel**) for various temperatures as provided by labels. The right-hand side endpoints "+" are for $\mu_B = 2000$ MeV. One could also combine the results of Figure 2 along cuts of $T = const$ to arrive at the same picture. The crosses depict results of the lattice QCD calculations [24] in both panels. The bullet depicts the onset point of the perturbative QCD regime for $T = 0$. Nuclear many-body theory is expected to apply below the left bottom corner.

4. Conclusions and Summary

Einstein–Maxwell-dilaton (EMd) models have become quite popular in the last few years. They are aimed at obtaining a quantified hint of the location of a (hypothetical) critical end point (CEP) and emerging first-order phase transition (FOPT) curve in the phase diagram of QCD. The experimental search in relativistic heavy-ion collisions and the conjectured impact on neutron star merger dynamics and compact (neutron) star configurations up to sources of stochastic gravitational waves formed in the cosmological confinement epoch provide strong motivation to apply the class of EMd models in a regime where direct first-principle QCD calculations are not (yet) at our disposal.

EMd models are argued to deliver reliable information in the deconfinement regime. Once the dilaton potential and the dynamical coupling are adjusted, a specific EMd model parameterization delivers as primary quantities the entropy density s and the baryon density n_B, thus allowing the construction of isobars $p = const$. These curves $T(\mu_B)|_{p=const}$ map the pressure profile, given by lattice QCD data on the temperature axis, onto the temperature–baryon–chemical potential plane towards the baryon–chemical potential axis. When supplemented with the available information on s and n_B, the accompanying energy density e and, thus, the warm equation of state $p(e)$ become accessible.

The model facilitates a critical end point and a peculiar first-order phase transition curve, which levels off partially due to an imposed optionally novel side condition to suppress the appearance of an unwanted purely thermal phase transition. Thus the pressure interval directly accessible by lattice QCD on the temperature axis is transformed to a pressure profile at smaller temperatures: $p(T, \mu_B = 0) \mapsto p(\text{smaller } T \approx 0, \mu_B > 0)$. We emphasize that the lattice QCD pressures in the temperature interval $T \in [125, 240]$ MeV continue (numerically) the equation of state of strong-interaction matter towards a region relevant for compact (neutron) stars and their merging dynamics but are not accessible reliably by nuclear many-body theory. We also emphasize that pressures $p(T \notin [125, 240]\ \mathrm{MeV}, \mu_B = 0)$ are largely unconstrained (and could be merely hampered by the employed ansätze of the dilaton potential and dynamical coupling of the EMd model), and, therefore, their mapping $p(T, \mu_B = 0) \mapsto p(T \approx 0, \mu_B)$ is hazardous, in contrast to the valuable control of pressures $p(T \in [125, 240]\ \mathrm{MeV}, \mu_B = 0) \mapsto p(T \in [125, 240]\ \mathrm{MeV}, \mu_B > 0)$ by lattice data with $0 < \mu_B/T \leq 3.5$.

Since the EMd model with our presently employed parameterization points to a peculiar shape of the first-order phase transition curve, one should test other ansätze to elucidate whether suitable side conditions have a strong impact. In a larger context, a systematic approach to reliable parameterizations of the dilaton potential and dynamical coupling within EMd models is desirable. The low-temperature–low-density behavior of the model appears somewhat mysterious and could point to the need of including explicitly fermionic degrees of freedom, i.e., nucleons and their hard-core repulsion. First-principle input would be highly welcome to better constrain the model and provide confidence at larger densities. For practical applications, however, that region is uncovered by nuclear many-body approaches, and the present model should be constrained to the high-density continuation relevant to compact stars. The matching to perturbative QCD is a further constraint to the holographic EoS to be considered in follow-up work towards a hybrid EoS, where, eventually, also local charge neutrality and β equilibrium should be imposed. In hybrid constructions [55], inhomogeneity effects [56] should also be accounted for. The role of the velocity of sound is to be emphasized [57–59] as well as the general finite-temperature behavior [60].

Author Contributions: Conceptualization, B.K.; methodology, B.K. and R.Z.; software, R.Z.; validation, R.Z. and B.K.; investigation, B.K. and R.Z.; writing—original draft preparation, B.K.; writing—review and editing, B.K. and R.Z.; visualization, R.Z.; supervision, B.K.; project administration, B.K. All authors have read and agreed to the published version of the manuscript.

Funding: The work is supported in part by the European Union's Horizon 2020 research and innovation program STRONG-2020 under grant agreement No. 824093.

Data Availability Statement: Publicly accessible lattice QCD data has been used to adjust our model to it by own software.

Acknowledgments: The authors are grateful to Sz. Borsányi for communications with respect to lattice QCD data. One author (BK) acknowledges conversations with J. Erdmenger, K. Redlich, and W. Weise.

Conflicts of Interest: The authors declare no conflicts of interest.

Appendix A. A Toy Model of Isobars

Figure A1 illustrates the envisioned mapping of the hot EoS, $p(T, \mu_B = 0)$, into the T-μ_B plane and eventually to the μ_B axis to arrive at the warm EoS, $p(T, \mu_B)$, and cool EoS, $p(T = 0, \mu_B)$, respectively, by a toy model. The mapping is accomplished generically by isobars, i.e., curves $p(T, \mu_B) = const$ determined by Equation (1). The displayed curves in Figure A1 are for a toy model with $p = aT^4 + bT^2\mu_B^2 + c\mu_B^4 + d$ implying $\hat{s} \equiv s/T^3 = 4a + 2b\hat{\mu}_B^2$, $\hat{n}_B \equiv n_B/T^3 = 4c\hat{\mu}_B^3 + 2b\hat{\mu}_B$ and numerical values $b/a = 0.02738$, $c/a = 0.000154$, which refer to a noninteracting two-flavor quark–gluon medium. Note that, in this special case of $\hat{s}$ and $\hat{n}_B$ depending only on $\hat{\mu}_B \equiv \mu_B/T$, an isobar starting at $T = T_0$ ends at $\mu_{B\,0} = 8.79\, T_0$. Isentropic trajectories, $T \propto \mu_B$ from $s/n_B = const$, miss the typical back-bending at $T = \mathcal{O}(150\ \mathrm{MeV})$ (see Figure 4 in [61], Figure 10 in [53], Figure 11 in [54], and Figure 4 in [62]), thus, evidencing the limited applicability of the toy model in the confinement region. In particular, a CEP and related FOPT curve are completely missed in this toy model.

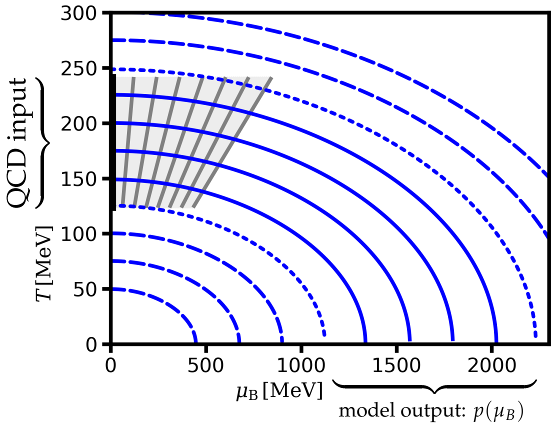

Figure A1. Illustration of expected isobars $p(T, \mu_B) = const$ over the T-μ_B plane in a toy model. The heavy solid bar on the T axis indicates the region, where reliable QCD input data (e.g., $p(T)$ and $\chi_2(T)$) are at our disposal. The continuation to $\mu_B > 0$ is controlled by lattice data in the hatched region (with sections of rays $\mu_B/T = const$ highlighted). Isobars not emerging from the heavy solid vertical bar or not running a noticeable section through the hatched control region are to be considered as less reliable (dashed or dotted curves). Irrespective of the EoS on the T axis, such a mapping by "laminar curves" $T(\mu_B)|_{p=const}$ (solid curves) would allow us to arrive unambiguously at the cool EoS at $T = 0$, or any other cut through the T-μ_B plane, thus also providing a warm EoS for neutron star merger dynamics.

Appendix B. Details of the EMd Model

The action (2) with the metric (3) leads to the field equations

$$A'' = -\frac{1}{6}\phi'^2, \tag{A1}$$

$$f'' = e^{-2A}\,\mathcal{G}\,\Phi'^2 - 4A'f', \tag{A2}$$

$$\phi'' = \frac{1}{f}\left(\partial_\phi V - \frac{1}{2}e^{-2A}\,\Phi'^2\,\partial_\phi\mathcal{G}\right) - \left(4A' + \frac{f'}{f}\right)\phi', \tag{A3}$$

$$\Phi'' = -2A'\phi' - \frac{\partial_\phi\mathcal{G}}{\mathcal{G}}\,\phi'\,\Phi', \tag{A4}$$

to be solved with boundary conditions

$$A(0) = 0, \qquad A'(0) = -\frac{1}{6}\Big(2V(\phi(0)) + \Phi_1^2\,\mathcal{G}(\phi(0))\Big), \tag{A1$'$}$$

$$f(0) = 0, \qquad f'(0) = 1, \tag{A2$'$}$$

$$\phi(0) = \phi_0, \qquad \phi'(0) = \partial_\phi V|_{\phi(0)} - \frac{1}{2}\Phi_1^2\,\partial_\phi\mathcal{G}|_{\phi(0)}, \tag{A3$'$}$$

$$\Phi(0) = 0, \qquad \Phi'(0) = \Phi_1, \tag{A4$'$}$$

where a prime means derivative with respect to coordinate r.

Entropy density and baryon density follow from (cf. [8])

$$s(T, \mu_B) = \frac{2\pi}{\kappa_5^2}\frac{1}{\phi_A^{3/\nu}}, \tag{A5}$$

$$n_B(T, \mu_B) = -\frac{1}{\kappa_5^2}\frac{\Phi_2^{\mathrm{far}}}{\phi_A^{3/\nu}\sqrt{f_0^{\mathrm{far}}}} \tag{A6}$$

with $T = 1/(4\pi L \phi_A^{1/\nu}\sqrt{f_0^{\text{far}}})$ and $\mu_B = 4\pi\, T\, \Phi_0^{\text{far}}$. The needed coefficients f_0^{far}, $\Phi_{0,2}^{\text{far}}$, and ϕ_A are obtained by adjusting the asymptotic series expansions near boundary,

$$f(r \to \infty) = f_0^{\text{far}} + \ldots, \tag{A7}$$

$$\phi(r \to \infty) = \phi_A e^{-\nu\alpha(r)} + \phi_B e^{-\Delta_\phi \alpha(r)} + \ldots, \tag{A8}$$

$$\Phi(r \to \infty) = \Phi_0^{\text{far}} + \Phi_2^{\text{far}} e^{-2\alpha(r)} + \ldots, \tag{A9}$$

to numerical solutions of Equations (A1)–(A4) with (A1′)–(A4′), together with the relations $\nu = 4 - \Delta_\phi$, $\Delta_\phi := 2(1 + \sqrt{1 - 3p_1})$ (cf. Equation (4) for p_1). Typical dependencies are $f_0^{\text{far}} \to T$, $\Phi_0^{\text{far}} \to \mu_B$, and $\Phi_2^{\text{far}} \to n_B$. We emphasize that using the coordinates (3) is numerically advantageous in comparison with the ones deployed in [50,63,64] since r-dependent quantities appear near boundary as exponentials (instead of power functions in the radial bulk coordinate z, $z \in [0, z_H]$), which is mainly favorable for the warp factor A.

In practice, we chose initial conditions set by ϕ_0 and Φ_1 to generate a rectangular grid over the T-μ_B plane. The pressure can be obtained either by a line integral with $p(T = 0, \mu_B = 0) = 0$ or by solving Equation (1) with proper boundary conditions at $p(T, \mu_B = 0)$ given by lattice QCD data. That is, $\mathrm{d}p = s\mathrm{d}T + n_B \mathrm{d}\mu_B$, $s = \partial p/\partial T$ and $n_B = \partial p/\partial \mu_B$, is exploited.

Appendix C. Density and Pressure at FOPT

Across the FOPT, the density makes a huge jump, as exhibited in the left panel of Figure A2. The FOPT curve is determined by the standard construction: find the self-crossing of the curve p/T^4 as a function of T at $\mu_B = const$. The abovementioned peculiarities are obvious in the right panel of Figure A2: small values of p/T^4, even for low temperatures, seemingly μ_B-independence of the low-temperature branch, and weak μ_B dependence of the high-temperature branch for $\mu_B \geq 1500$ MeV. The squeezing of curves $p = const$ into a narrow corridor right up to the FOPT curve (see left panel of Figure 3 or right panel of Figure 2 for p/T^4) is a consequence of the initial steep increase of the high-temperature branch with T.

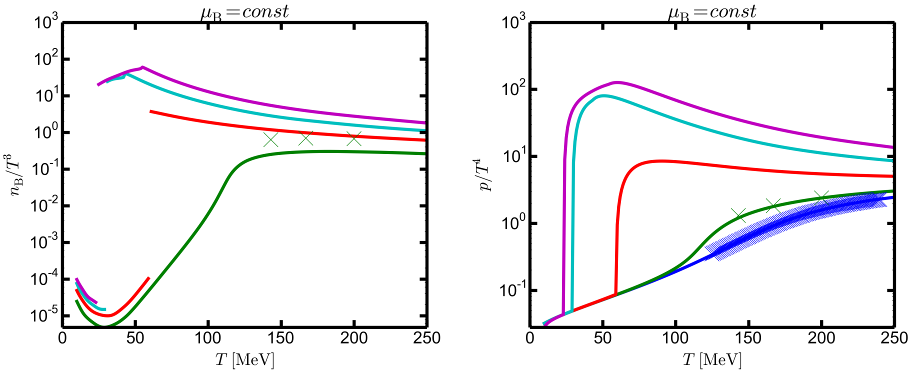

Figure A2. The stable branches of scaled density n_B/T^3 (left panel) and scaled pressure p/T^4 as a function of temperature T for various values of $\mu_B = n\,500$ MeV for $n = 0$ (blue), 1 (green), 2 (red), 3 (cyan), and 4 (magenta). The crosses depict the results of the lattice QCD calculations [24].

Upon inspecting the right panel of Figure A2, note (i) the log scale, (ii) the apparent independence of the low-temperature branch on μ_B (see also left panel in Figure 3), and (iii) the weak μ_B dependence of the high-temperature branches for $\mu_B \geq 1500$ MeV which causes the leveling off of the FOPT curve $T_{\text{FOPT}}(\mu_B)$; see black curves in Figures 2 and 3. For some guidance, one could resort to the Hadron resonance gas model of confined strong-interaction matter with full quantum statistics and vacuum rest masses. Of course, the pion gas pressure $p = \frac{3}{2\pi^2} m_\pi^2 T^2 \sum_{\ell=1}^{\infty} \ell^{-2} K_2(\frac{\ell m_\pi}{T})$ is independent of μ_B; it is numerically consistent with the EMd behavior for $T \in [50, 100]$ MeV, but falls significantly short at

$T < 50$ MeV. Adding a nucleon Fermi gas at $\mu_B = 500$ MeV semiquantitatively explains the rise of the pressure at $T > 100$ MeV relative to the $\mu_B = 0$ curve. All that seems elucidate the failure of such a naive interpretation of the EMd results.

Appendix D. Various Dilaton Potential Parameterizations

Lacking a strict gravity dual of QCD, one adjusts, in bottom-up approaches, the dilaton potential at suitable QCD input. General guidelines are described in [65] and used in [5]. Practitioners would prefer to utilize a less theory-based ansatz and extend the set of parameters to be fixed to numerically catch the wanted quantities, as performed in Equation (4). Another dilaton potential ansatz is proposed in [13]; it differs from the ansatz in [8,11,12]. When inspecting plots (not displayed) of the dilaton potential function $\mathcal{W}(\phi) = \mathrm{d}\log V(\phi)/\mathrm{d}\phi$, one recognizes that [10–13] look strikingly the same for $\phi < 3.5$: they display a maximum of $\mathcal{W}_m \approx 0.6$ at $\phi_m \approx 3.25$. In adiabatic approximation, the maximum corresponds to the minimum of squared sound velocity, $v_s^2 \approx \frac{1}{3} - \frac{1}{2}\mathcal{W}$. The mentioned dilaton potentials can be well fitted by our ansatz Equation (4) with some spread of the coefficients $p_{1,2,3,}$ and γ. The two side conditions make $\mathcal{W}(\phi)$ dependent on p_1 (which fixes the dynamical dimension Δ_ϕ) and γ: $p_2 = (-2p_1\phi_m + \mathcal{W}_m \exp\{\gamma\phi_m\}[3 - \gamma\phi_m])/\phi_m^2$ and $p_3 = (p_1\phi_m - \mathcal{W}_m \exp\{\gamma\phi_m\}[2 - \gamma\phi_m])/\phi_m^3$. The corresponding contour plots of χ^2 with respect to scaled entropy density, L^{-1}, and κ_5 are exhibited in Figure A3. We define $\chi^2 = \sum_{n=1}^{24}(s/T^3|_{n\,lattice} - s/T^3|_{T_n\,\mathcal{W}(p_1,\gamma)})^2/(\delta s/T^3|_{n\,lattice})^2$ with symmetrized error bars $\delta s/T^3|_{n\,lattice}$ at the 24 values T_n of lattice data [24]. At each point (p_1, γ), χ^2 is minimized by free and independent variations of L and κ_5. Surprising is the wide variation of the scale setting parameter L^{-1}, while $\kappa_5/L^{3/2} \approx 1.87$. The flickering χ^2 contours are understood as the result of biasing the fit problem by fixing the maximum of $\mathcal{W}$ at $\phi_m = 3.25$, which flattens the χ^2 landscape. The left panel in Figure A3 suggests that our choice of the ansatz and parameters in Equation (4) is not the optimal one when prescribing $\mathcal{W}_m = 0.6$ at $\phi_m = 3.25$. However, the real χ^2 minimum requires a scan through the full $(p_{1,2,3}, \gamma, L, \kappa_5)$ space without constraints, preferentially including other observables, too.

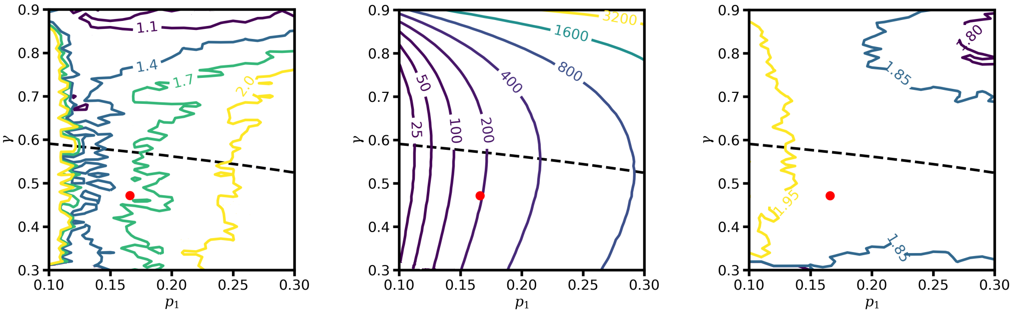

Figure A3. Contour plots of χ^2 with respect to scaled entropy density (**left panel**), L^{-1} (**middle panel**), and κ_5 (**right panel**, in units of $L^{3/2}$) for the dilaton potential function Equation (4) with local maximum of $\mathcal{W}_m = 0.6$ at $\phi_m = 3.25$ as side conditions. The dashed line depicts the locus of $p_3 = 0$ determined by $p_1 = \mathcal{W}_m \exp\{\gamma\phi_m\}(2 - \gamma\phi_m)/\phi_m$, i.e., for $p_3 > 0$, an unintended thermal phase transition is excluded since, beyond the maximum, $\mathcal{W}(\phi)$ is smoothly and monotonously approaching zero at $\phi \to \infty$. The bullet in the $p_3 < 0$ region is for the parameter choice of $p_{1,2,3}$ and γ listed below Equation (5), which facilitates $\mathcal{W}_m \approx 0.6$ at $\phi_m \approx 3.25$.

The dilaton parameterizations proposed in [23,46], which also nicely reproduce the lattice QCD data, cannot be described quantitatively by our ansatz Equation (4) in the range $\phi = 0$ up to and including the first local maximum of $\mathcal{W}$.

References

1. Abbott, B.P.; Abbott, R.; Abbott, T.D.; Abraham, S.; Acernese, F.; Ackley, K.; Adams, C.; Adhikari, R.X.; Adya, V.B.; Affeldt, C.; et al. [LIGO Scientific and Virgo]. GW190425: Observation of a Compact Binary Coalescence with Total Mass $\sim 3.4 M_{\odot}$. *Astrophys. J. Lett.* **2020**, *892*, L3. [CrossRef]
2. Miller, M.C.; Lamb, F.K.; Dittmann, A.J.; Bogdanov, S.; Arzoumanian, Z.; Gendreau, K.C.; Guillot, S.; Harding, A.K.; Ho, W.C.G.; Lattimer, J.M.; et al. PSR J0030 + 0451 Mass and Radius from *NICER* Data and Implications for the Properties of Neutron Star Matter. *Astrophys. J. Lett.* **2019**, *887*, L24. [CrossRef]
3. Riley, T.E.; Watts, A.L.; Bogdanov, S.; Ray, P.S.; Ludlam, R.M.; Guillot, S.; Arzoumanian, Z.; Baker, C.L.; Bilous, A.V.; Chakrabarty, D.; et al. A *NICER* View of PSR J0030 + 0451: Millisecond Pulsar Parameter Estimation. *Astrophys. J. Lett.* **2019**, *887*, L21. [CrossRef]
4. Miller, M.C.; Lamb, F.K.; Dittmann, A.J.; Bogdanov, S.; Arzoumanian, Z.; Gendreau, K.C.; Guillot, S.; Ho, W.C.G.; Lattimer, J.M.; Loewenstein, M.; et al. The Radius of PSR J0740+6620 from NICER and XMM-Newton Data. *Astrophys. J. Lett.* **2021**, *918*, L28. [CrossRef]
5. Järvinen, M. Holographic modeling of nuclear matter and neutron stars. *Eur. Phys. J. C* **2022**, *82*, 282. [CrossRef]
6. Hoyos, C.; Jokela, N.; Vuorinen, A. Holographic approach to compact stars and their binary mergers. *Prog. Part. Nucl. Phys.* **2022**, *126*, 103972. [CrossRef]
7. Chesler, P.M.; Jokela, N.; Loeb, A.; Vuorinen, A. Finite-temperature Equations of State for Neutron Star Mergers. *Phys. Rev. D* **2019**, *100*, 066027. [CrossRef]
8. DeWolfe, O.; Gubser, S.S.; Rosen, C. A holographic critical point. *Phys. Rev. D* **2011**, *83*, 086005. [CrossRef]
9. DeWolfe, O.; Gubser, S.S.; Rosen, C. Dynamic critical phenomena at a holographic critical point. *Phys. Rev. D* **2011**, *84*, 126014. [CrossRef]
10. Cai, R.G.; He, S.; Li, L.; Wang, Y.X. Probing QCD critical point and induced gravitational wave by black hole physics. *Phys. Rev. D* **2022**, *106*, L121902. [CrossRef]
11. Grefa, J.; Noronha, J.; Noronha-Hostler, J.; Portillo, I.; Ratti, C.; Rougemont, R. Hot and dense quark-gluon plasma thermodynamics from holographic black holes. *Phys. Rev. D* **2021**, *104*, 034002. [CrossRef]
12. Critelli, R.; Noronha, J.; Noronha-Hostler, J.; Portillo, I.; Ratti, C.; Rougemont, R. Critical point in the phase diagram of primordial quark-gluon matter from black hole physics. *Phys. Rev. D* **2017**, *96*, 096026. [CrossRef]
13. Knaute, J.; Yaresko, R.; Kämpfer, B. Holographic QCD phase diagram with critical point from Einstein–Maxwell-dilaton dynamics. *Phys. Lett. B* **2018**, *778*, 419–425. [CrossRef]
14. Jokela, N.; Järvinen, M.; Remes, J. Holographic QCD in the NICER era. *Phys. Rev. D* **2022**, *105*, 086005. [CrossRef]
15. Demircik, T.; Ecker, C.; Järvinen, M. Dense and Hot QCD at Strong Coupling. *Phys. Rev. X* **2022**, *12*, 041012. [CrossRef]
16. Ishii, T.; Järvinen, M.; Nijs, G. Cool baryon and quark matter in holographic QCD. *J. High Energy Phys.* **2019**, *2019*, 3. [CrossRef]
17. Tootle, S.; Ecker, C.; Topolski, K.; Demircik, T.; Järvinen, M.; Rezzolla, L. Quark formation and phenomenology in binary neutron-star mergers using V-QCD. *SciPost Phys.* **2023**, *13*, 109. [CrossRef]
18. Demircik, T.; Ecker, C.; Järvinen, M.; Rezzolla, L.; Tootle, S.; Topolski, K. Exploring the Phase Diagram of V-QCD with Neutron Star Merger Simulations. *EPJ Web Conf.* **2022**, *274*, 07006. [CrossRef]
19. Grefa, J.; Hippert, M.; Noronha, J.; Noronha-Hostler, J.; Portillo, I.; Ratti, C.; Rougemont, R. Transport coefficients of the quark-gluon plasma at the critical point and across the first-order line. *Phys. Rev. D* **2022**, *106*, 034024. [CrossRef]
20. Hoyos, C.; Jokela, N.; Järvinen, M.; Subils, J.G.; Tarrio, J.; Vuorinen, A. Holographic approach to transport in dense QCD matter. *Phys. Rev. D* **2022**, *105*, 066014. [CrossRef]
21. Zhang, L.; Huang, M. Holographic cold dense matter constrained by neutron stars. *Phys. Rev. D* **2022**, *106*, 096028. [CrossRef]
22. Rougemont, R.; Grefa, J.; Hippert, M.; Noronha, J.; Noronha-Hostler, J.; Portillo, I.; Ratti, C. Hot QCD phase diagram from holographic Einstein–Maxwell–Dilaton models. *Prog. Part. Nucl. Phys.* **2024**, *135*, 104093. [CrossRef]
23. Jokela, N.; Järvinen, M.; Piispa, A. Refining holographic models of the quark-gluon plasma. *arXiv* **2024**, arXiv:2405.02394.
24. Borsányi, S.; Fodor, Z.; Guenther, J.N.; Kara, R.; Katz, S.D.; Parotto, P.; Pásztor, A.; Ratti, C.; Szabó, K.K. Lattice QCD equation of state at finite chemical potential from an alternative expansion scheme. *Phys. Rev. Lett.* **2021**, *126*, 232001. [CrossRef] [PubMed]
25. Bazavov, A.; Bhattacharya, T.; DeTar, C.; Ding, H.T.; Gottlieb, S.; Gupta, R.; Hegde, P.; Heller, U.M.; Karsch, F.; Laermann, E.; et al. Equation of state in (2 + 1)-flavor QCD. *Phys. Rev. D* **2014**, *90*, 094503. [CrossRef]
26. Borsanyi, S.; Fodor, Z.; Hoelbling, C.; Katz, S.D.; Krieg, S.; Szabo, K.K. Full result for the QCD equation of state with 2 + 1 flavors. *Phys. Lett. B* **2014**, *730*, 99–104. [CrossRef]
27. Bazavov, A.; Ding, H.T.; Hegde, P.; Kaczmarek, O.; Karsch, F.; Laermann, E.; Maezawa, Y.; Mukherjee, S.; Ohno, H.; Petreczky, P.; et al. The QCD Equation of State to $\mathcal{O}(\mu_B^6)$ from Lattice QCD. *Phys. Rev. D* **2017**, *95*, 054504. [CrossRef]
28. Borsanyi, S.; Guenther, J.N.; Kara, R.; Fodor, Z.; Parotto, P.; Pasztor, A.; Ratti, C.; Szabo, K.K. Resummed lattice QCD equation of state at finite baryon density: Strangeness neutrality and beyond. *Phys. Rev. D* **2022**, *105*, 114504. [CrossRef]
29. Bollweg, D.; Clarke, D.A.; Goswami, J.; Kaczmarek, O.; Karsch, F.; Mukherjee, S.; Petreczky, P.; Schmidt, C.; Sharma, S.; (HotQCD Collaboration). Equation of state and speed of sound of (2 + 1)-flavor QCD in strangeness-neutral matter at nonvanishing net baryon-number density. *Phys. Rev. D* **2023**, *108*, 014510. [CrossRef]
30. Ecker, C.; Rezzolla, L. Impact of large-mass constraints on the properties of neutron stars. *Mon. Not. R. Astron. Soc.* **2022**, *519*, 2615–2622. [CrossRef]

31. Annala, E.; Gorda, T.; Katerini, E.; Kurkela, A.; Nättilä, J.; Paschalidis, V.; Vuorinen, A. Multimessenger Constraints for Ultradense Matter. *Phys. Rev. X* **2022**, *12*, 011058. [CrossRef]
32. Hebeler, K.; Lattimer, J.M.; Pethick, C.J.; Schwenk, A. Equation of state and neutron star properties constrained by nuclear physics and observation. *Astrophys. J.* **2013**, *773*, 11. [CrossRef]
33. Stephanov, M.A.; Rajagopal, K.; Shuryak, E.V. Event-by-event fluctuations in heavy ion collisions and the QCD critical point. *Phys. Rev. D* **1999**, *60*, 114028. [CrossRef]
34. Karsch, F. Lattice QCD at high temperature and density. *Lect. Notes Phys.* **2002**, *583*, 209–249.
35. Fukushima, K.; Hatsuda, T. The phase diagram of dense QCD. *Rept. Prog. Phys.* **2011**, *74*, 014001. [CrossRef]
36. Halasz, A.M.; Jackson, A.D.; Shrock, R.E.; Stephanov, M.A.; Verbaarschot, J.J.M. On the phase diagram of QCD. *Phys. Rev. D* **1998**, *58*, 096007. [CrossRef]
37. Almaalol, D.; Hippert, M.; Noronha-Hostler, J.; Noronha, J.; Speranza, E.; Basar, G.; Bass, S.; Cebra, D.; Dexheimer, V.; Keane, D.; et al. QCD Phase Structure and Interactions at High Baryon Density: Continuation of BES Physics Program with CBM at FAIR. *arXiv* **2022**, arXiv:2209.05009.
38. Du, L.; Sorensen, A.; Stephanov, M. The QCD phase diagram and Beam Energy Scan physics: A theory overview. *arXiv* **2024**, arXiv:2402.10183.
39. Lovato, A.; Dore, T.; Pisarski, R.D.; Schenke, B.; Chatziioannou, K.; Read, J.S.; Landry, P.; Danielewicz, P.; Lee, D.; Pratt, S.; et al. Long Range Plan: Dense matter theory for heavy-ion collisions and neutron stars. *arXiv* **2022**, arXiv:2211.02224.
40. Kumar, R.; Dexheimer, V.; Jahan, J.; Noronha, J.; Noronha-Hostler, J.; Ratti, C.; Yunes, N.; Acuna, A.R.N.; Alford, M.; Anik, M.H.; et al. Theoretical and Experimental Constraints for the Equation of State of Dense and Hot Matter. *arXiv* **2023**, arXiv:2303.17021.
41. Fujimoto, Y.; Fukushima, K.; McLerran, L.D.; Praszalowicz, M. Trace Anomaly as Signature of Conformality in Neutron Stars. *Phys. Rev. Lett.* **2022**, *129*, 252702. [CrossRef]
42. Marczenko, M.; McLerran, L.; Redlich, K.; Sasaki, C. Reaching percolation and conformal limits in neutron stars. *Phys. Rev. C* **2023**, *107*, 025802. [CrossRef]
43. Pradeep, M.S.; Sogabe, N.; Stephanov, M.; Yee, H.U. Non-monotonic specific entropy on the transition line near the QCD critical point. *arXiv* **2024**, arXiv:2402.09519.
44. He, S.; Li, L.; Wang, S.; Wang, S.J. Constraints on holographic QCD phase transitions from PTA observations. *arXiv* **2023**, arXiv:2308.07257.
45. Middeldorf-Wygas, M.M.; Oldengott, I.M.; Bödeker, D.; Schwarz, D.J. Cosmic QCD transition for large lepton flavor asymmetries. *Phys. Rev. D* **2022**, *105*, 123533. [CrossRef]
46. Hippert, M.; Grefa, J.; Manning, T.A.; Noronha, J.; Noronha-Hostler, J.; Vazquez, I.P.; Ratti, C.; Rougemont, R.; Trujillo, M. Bayesian location of the QCD critical point from a holographic perspective. *arXiv* **2023**, arXiv:2309.00579.
47. Bellwied, R.; Borsanyi, S.; Fodor, Z.; Katz, S.D.; Pasztor, A.; Ratti, C.; Szabo, K.K. Fluctuations and correlations in high temperature QCD. *Phys. Rev. D* **2015**, *92*, 114505. [CrossRef]
48. Yaresko, R.; Knaute, J.; Kämpfer, B. Cross-over versus first-order phase transition in holographic gravity–single-dilaton models of QCD thermodynamics. *Eur. Phys. J. C* **2015**, *75*, 295. [CrossRef]
49. Zöllner, R.; Kämpfer, B. Phase structures emerging from holography with Einstein gravity—dilaton models at finite temperature. *Eur. Phys. J. Plus* **2020**, *135*, 304. [CrossRef]
50. Zöllner, R.; Ding, M.; Kämpfer, B. Masses of compact (neutron) stars with distinguished cores. *Particles* **2023**, *6*, 217–238. [CrossRef]
51. Gao, F.; Pawlowski, J.M. Chiral phase structure and critical end point in QCD. *Phys. Lett. B* **2021**, *820*, 136584. [CrossRef]
52. Bernhardt, J.; Fischer, C.S.; Isserstedt, P.; Schaefer, B.J. Critical endpoint of QCD in a finite volume. *Phys. Rev. D* **2021**, *104*, 074035. [CrossRef]
53. Karthein, J.M.; Mroczek, D.; Acuna, A.R.N.; Noronha-Hostler, J.; Parotto, P.; Price, D.R.P.; Ratti, C. Strangeness-neutral equation of state for QCD with a critical point. *Eur. Phys. J. Plus* **2021**, *136*, 621. [CrossRef]
54. Parotto, P.; Bluhm, M.; Mroczek, D.; Nahrgang, M.; Noronha-Hostler, J.; Rajagopal, K.; Ratti, C.; Schäfer, T.; Stephanov, M. QCD equation of state matched to lattice data and exhibiting a critical point singularity. *Phys. Rev. C* **2020**, *101*, 034901. [CrossRef]
55. Blacker, S.; Bauswein, A. Comprehensive survey of hybrid equations of state in neutron star mergers and constraints on the hadron-quark phase transition. *arXiv* **2024**, arXiv:2406.14669.
56. Demircik, T.; Jokela, N.; Jarvinen, M.; Piispa, A. Is holographic quark-gluon plasma homogeneous? *arXiv* **2024**, arXiv:2405.02392.
57. Hippert, M.; Noronha, J.; Romatschke, P. Upper Bound on the Speed of Sound in Nuclear Matter from Transport. *arXiv* **2024**, arXiv:2402.14085.
58. Yao, N.; Sorensen, A.; Dexheimer, V.; Noronha-Hostler, J. Structure in the speed of sound: From neutron stars to heavy-ion collisions. *Phys. Rev. C* **2024**, *109*, 065803. [CrossRef]
59. Rojas, J.C.; Demircik, T.; Järvinen, M. Popcorn Transitions and Approach to Conformality in Homogeneous Holographic Nuclear Matter. *Symmetry* **2023**, *15*, 331. [CrossRef]
60. Mroczek, D.; Yao, N.; Zine, K.; Noronha-Hostler, J.; Dexheimer, V.; Haber, A.; Most, E.R. Finite-temperature expansion of the dense-matter equation of state. *arXiv* **2024**, arXiv:2404.01658.
61. Flor, F.A.; Olinger, G.; Bellwied, R. Flavour and Energy Dependence of Chemical Freeze-out Temperatures in Relativistic Heavy Ion Collisions from RHIC-BES to LHC Energies. *Phys. Lett. B* **2021**, *814*, 136098. [CrossRef]

62. Günther, J.; Bellwied, R.; Borsanyi, S.; Fodor, Z.; Katz, S.D.; Pasztor, A.; Ratti, C. The QCD equation of state at finite density from analytical continuation. *EPJ Web Conf.* **2017**, *137*, 07008. [CrossRef]
63. Zöllner, R.; Kämpfer, B. Quarkonia Formation in a Holographic Gravity–Dilaton Background Describing QCD Thermodynamics. *Particles* **2021**, *4*, 159–177. [CrossRef]
64. Zöllner, R.; Kämpfer, B. Holographic bottomonium formation in a cooling strong-interaction medium at finite baryon density. *Phys. Rev. D* **2021**, *104*, 106005. [CrossRef]
65. Gursoy, U.; Kiritsis, E.; Mazzanti, L.; Michalogiorgakis, G.; Nitti, F. Improved Holographic QCD. *Lect. Notes Phys.* **2011**, *828*, 79–146.